

---

# Learning disentangled representations via product manifold projection

---

Marco Fumero<sup>1</sup> Luca Cosmo<sup>1,2</sup> Simone Melzi<sup>1</sup> Emanuele Rodolà<sup>1</sup>

## Abstract

We propose a novel approach to disentangle the generative factors of variation underlying a given set of observations. Our method builds upon the idea that the (unknown) low-dimensional manifold underlying the data space can be explicitly modeled as a product of submanifolds. This gives rise to a new definition of disentanglement, and to a novel weakly-supervised algorithm for recovering the unknown explanatory factors behind the data. At training time, our algorithm only requires pairs of non i.i.d. data samples whose elements share at least one, possibly multidimensional, generative factor of variation. We require no knowledge on the nature of these transformations, and do not make any limiting assumption on the properties of each subspace. Our approach is easy to implement, and can be successfully applied to different kinds of data (from images to 3D surfaces) undergoing arbitrary transformations. In addition to standard synthetic benchmarks, we showcase our method in challenging real-world applications, where we compare favorably with the state of the art.

## 1. Introduction

Human intelligence is often understood as a process of turning experience into new behavior, knowledge, and skills. Humans achieve this by constructing small models of the world in their brains to explain the sensory experience and use them to infer new consequences. These models can be understood as turning experience into compact representations: functions of the experienced data which are useful for a given task. Representation learning (Bengio et al., 2014) aims to mimic this process with machines, via studying and formalizing what makes a good representation of high dimensional data, and how can we compute it in the form of an algorithm. A central topic in this research field is *disentan-*

*gled* representations, which advocates that a representation of an entity should capture the different latent factors of variation in the world where that entity is observed. This abstract concept has led to several formalizations, but the community has not yet settled on a common definition.

In this work, we propose a new definition of disentanglement, based on the concept of projection over product spaces, and we provide an algorithm to compute disentangled representations by a weakly supervised approach. Since we do not require much knowledge of the data and their variations, our method fits different applications. Our main contributions can be summarized as follows:

- We introduce a new definition of disentanglement, which relies on geometric notions, and we show that our theoretical framework entails a generalization of current approaches.
- Relying on assumptions of the sample distribution, we provide a weakly supervised recipe that is simple to integrate into standard neural network models.
- We widely test our approach on synthetic datasets and more challenging real-world scenarios, outperforming the state of the art in several cases.

### 1.1. Related work

The task of identifying the underlying factors of variation in the data has been a primary goal in representation learning research (Bengio et al., 2014).

The problem of recovering independent components in a generative process relates to the independent component analysis (ICA). Given a multivariate signal, ICA aims to separate it into additive elements generated by independent non-Gaussian sources (Comon, 1994). While in the non-linear case, observing i.i.d. samples, ICA was proven to be unidentifiable (Hyvärinen & Pajunen, 1999), recent approaches (Hyvärinen et al., 2019; Hyvärinen & Morioka, 2016) have built on the assumption of having some degree of supervision to couple ICA and disentanglement.

A recent and promising line of research (Higgins et al., 2017; Kumar et al., 2018; Chen et al., 2019; Kim & Mnih, 2019) aimed to attain disentanglement in a fully unsupervised way, relying on a probabilistic interpretation according to which

---

<sup>1</sup>Sapienza, University of Rome, Rome, Italy <sup>2</sup>Università della Svizzera italiana, Lugano, Switzerland. Correspondence to: Marco Fumero <fumero@di.uniroma1.it>.

a representation is defined to be disentangled if the data distribution can be modeled as a nonlinear transformation of a product of independent probability distributions. Unfortunately, similarly to the ICA case, this leads to pessimistic results (Locatello et al., 2019) in terms of the identifiability of the factors without any assumptions on the model or the data (inductive bias). In this work we propose a different definition of disentanglement, which is entirely based on the geometric notion of metric and manifolds, and we rely on the assumption on observing non i.i.d. samples as data – thus escaping the non-identifiability result of (Locatello et al., 2019).

A more general definition of disentanglement in terms of group theory was given in (Higgins et al., 2018). Under their definition, a representation is disentangled if it matches the product of groups that define the symmetries in the world, i.e. if the representation decomposes in such a way that the action of a single subgroup leaves all factors of the representation invariant except for one. A first practical tentative in this direction was proposed by Pfau et al. (2020), which aims to discover a decomposition of a data manifold by investigating its holonomy group; but in order to work properly, the method requires to have full access to the metric of the data manifold. Differently, we provide a simple algorithm to obtain a disentangled representation in the form of a plug-in module for any autoencoder model.

By allowing supervision, one can escape to some extent the limitations underlined by Locatello et al. (2019), trading off identifiability of the model with scalability to realistic settings. The latter is due to the absence of labelled data in real scenarios. Supervision in disentanglement may come in different flavors, from weakly supervised settings (Locatello et al., 2020a; Shu et al., 2020), to semi-supervised (Locatello et al., 2020b) and fully supervised approaches (Kazemi et al., 2019). We position our work in the weakly supervised setting; we assume to observe non i.i.d. sample pairs which differ only by a projection on a single submanifold.

Closer to our work is the line of research on manifold learning, a generalization of the classical field of linear dimensionality reduction to the nonlinear setting (Tenenbaum et al., 2000; van der Maaten & Hinton, 2008; Belkin & Niyogi, 2002; Roweis & Saul, 2000; McInnes et al., 2018). This line of works arises from the assumption that we observe the data in a high-dimensional Euclidean space  $\mathcal{X} \subset \mathbb{R}^N$  sampled from a low-dimensional manifold  $\mathcal{M}$ , which can be approximately embedded into a low-dimensional Euclidean space  $\mathcal{Z}$ . We make this assumption stronger, by conjecturing that the data manifold is factorizable into a product of subspaces; each subspace models a generative factor of the data.

## 2. Theoretical justification

At the basis of our work is the assumption that high-dimensional data lie near a low-dimensional manifold, and that this can be factored into a product of submanifolds, each modelling one factor of variation. This factorization is not unique. We aim to find the one that best explains the data while being semantically valid, i.e. interpretable by humans. Let  $\mathcal{M} = \mathcal{M}_1 \times \mathcal{M}_2 \times \dots \times \mathcal{M}_k$  be the product manifold we want to approximate. In this context, we only have access to observations of  $\mathcal{M} \subset \mathbb{R}^d$  in the high-dimensional space  $\mathcal{X} = \mathbb{R}^N$ , with  $N \gg d$ .

### 2.1. Background

Our definition of disentanglement is based upon the notion of metric. The manifold  $\mathcal{M}$  is equipped with a metric  $g_x : \mathcal{T}_x \mathcal{M} \times \mathcal{T}_x \mathcal{M} \rightarrow \mathbb{R}$ , where  $\mathcal{T}_x \mathcal{M}$  is the tangent space at  $x \in \mathcal{M}$ ;  $g_x$  is a smoothly varying function that enables the computation of lengths, angles and areas on the manifold. In particular, the distance between two arbitrary points  $x, y$  on the manifold is defined in terms of the metric tensor:  $d^2(x, y) = \int_0^1 g_{\gamma_t}(\dot{\gamma}_t, \dot{\gamma}_t) dt$  where  $\gamma : [0, 1] \rightarrow \mathcal{M}$  is a geodesic parametrized curve with  $\gamma(0) = x$  and  $\gamma(1) = y$ .

Since the metric allows us to compute distances, we can alternatively regard  $\mathcal{M}$  as a metric space. To define distances on a *product* manifold, we recall the following definition for product metric spaces:

**Definition 1 (Product metric space)** A *product metric space* is an ordered pair  $(M, d)$  where  $M$  is product of sets  $M_1 \times \dots \times M_k$  each equipped with a function  $d_i : M_i \times M_i \rightarrow \mathbb{R}$ ,  $\forall i$  s.t.  $\forall x, y, z \in M_i$ :

$$\begin{aligned} d_i(x, y) &= 0 \iff x = y \\ d_i(x, y) &= d_i(y, x) \\ d_i(x, z) &\leq d_i(x, y) + d_i(y, z) \end{aligned}$$

The metric on the product space corresponds to the  $L_2$  norm of the metric on the subspaces.

Distances on a product manifold can then be factored into the sum of distances on the submanifolds, since the metric of the product manifold simply reduces to the sum of the metrics of its constituents  $g(u, v) = \sum_i^K g_i(u_i, v_i)$ , resulting in a product metric space.

### 2.2. Disentangled representations

We define a representation as *disentangled* if the variation of one generative factor in the data corresponds to a change in *exactly one* submanifold. Let us be given two data samples, and assume one of them is transformed by some unknown process. Then, the change in the distance between their projections onto the product manifold, measured before

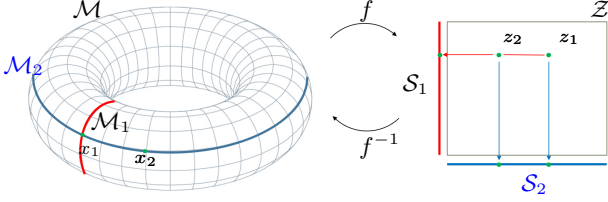


Figure 1. Let  $\mathcal{X} \subset \mathbb{R}^3$  be our input space composed by points lying near a 2-dimensional torus  $\mathcal{M}$ . Since the torus is a product manifold of two circles, we can represent points on the torus as projections on the two submanifolds  $\mathcal{M}_1$  and  $\mathcal{M}_2$ . Let  $f : \mathcal{X} \rightarrow \mathcal{Z}$  be an embedding into a subset of the plane  $\mathcal{Z} \subset \mathbb{R}^2$ .  $\mathcal{Z}$  can be factored into two subspaces  $\mathcal{S}_1 \subset \mathbb{R}$  and  $\mathcal{S}_2 \subset \mathbb{R}$ , which reflect the metric structure of  $\mathcal{M}_1, \mathcal{M}_2$ .

and after transforming the sample, is nonzero only on one submanifold. Thus, changing one factor of variation at a time will correspond to moving along a trajectory on a specific submanifold, while standing still on all the others.

Formally:

**Definition 2** Let  $\mathcal{M} = \mathcal{M}_1 \times \mathcal{M}_2 \times \dots \times \mathcal{M}_k$  be a product manifold embedded in high dimensional space  $\mathcal{X}$ . A representation  $z=f(x)$  in some space  $\mathcal{Z} = \mathcal{S}_1 \times \dots \times \mathcal{S}_k$ , s.t.  $\dim(\mathcal{Z}) \ll \dim(\mathcal{X})$ , is disentangled w.r.t.  $\mathcal{M}$  if there exists a smooth invertible function, with smooth inverse (a diffeomorphism)  $g : \mathcal{Z} \rightarrow \mathcal{M}$  s.t.  $\forall i \in 1, \dots, k; \forall a, b \in \mathcal{M}_i; \forall s_1, s_2 \in \mathcal{S}_i \subset \mathcal{Z}$ :

$$\begin{aligned} f &\approx g^{-1} \text{ on } \mathcal{M} \\ d_{\mathcal{M}_i}(a, b) > 0 &\implies d_{\mathcal{S}_i}(s_1, s_2) > 0 \\ d_{\mathcal{M}_i}(a, b) = 0 &\implies d_{\mathcal{S}_i}(s_1, s_2) = 0 \implies s_1 = s_2 \\ d_{\mathcal{M}_i}(a, b) &\approx d_{\mathcal{S}_i}(s_1, s_2) \end{aligned}$$

where  $s_j = \Pi_i g^{-1}(x_j)$  and  $\Pi_i$  denotes the projection onto the subspace  $\mathcal{S}_i \subset \mathcal{Z}$ .

The existence of  $g^{-1}$  is guaranteed by the Whitney immersion theorem (Whitney, 1936), which states that for any manifold of dimension  $m$  there exists a one-to-one mapping in a Euclidean space of dimension at least  $2m$  ( $2m - 1$  if the manifold is smooth). In addition, by Nash-Kuiper embedding theorem (Nash, 1956) this can be done isometrically, i.e. without any metric distortion, which addresses the last point of the definition.

**Example.** To better understand the definition we refer the reader to Figure 1, which allows us to introduce some notation. Let  $\mathcal{X} \supset \mathcal{M}$  be our observation space, equipped with the standard Euclidean metric  $d_e(\cdot, \cdot) = \|\cdot - \cdot\|_2$ . We consider the embedding function  $f : \mathcal{X} \rightarrow \mathcal{Z}$ , s.t.  $f \approx g^{-1}$ , where  $\mathcal{Z}$  is equipped with the metric induced via  $f$  and  $\dim(\mathcal{Z}) \ll \dim(\mathcal{X})$ . We consider the factorization  $\mathcal{Z} = \mathcal{S}_1 \times \dots \times \mathcal{S}_K$ , where each subspace ideally corresponds

to a parametric space for each of the  $\mathcal{M}_i \subset \mathcal{M}$ . We name the projections onto  $\mathcal{S}_i$  as  $\Pi_i : \mathcal{Z} \rightarrow \mathcal{S}_i \forall i \in \{1 \dots K\}$ . In Figure 1, the subsets  $\mathcal{S}_1, \mathcal{S}_2$  approximate the metric structure of  $\mathcal{M}_1, \mathcal{M}_2$  in the sense of Definition 2:  $z_1, z_2$  projected onto  $\mathcal{S}_1$  will correspond to the same point (i.e. their distance will be zero), reflecting the structure of  $\mathcal{M}_1$ , while their projection onto  $\mathcal{S}_2$  will approximate the distance of  $x_1, x_2$  on  $\mathcal{M}_2$ .

Furthermore, we can regard  $x_2$  as the result of a transformation  $T$  applied to  $x_1$ , namely a translation on the submanifold  $\mathcal{M}_2$  (in general, each pair of samples from  $\mathcal{M}$  can be seen in this sense). This allows us to describe the example of Figure 1 via the commutative diagrams in Figure 2.

$$\begin{array}{ccc} x_1 & \xrightarrow{f} & z_1 \xrightarrow{\Pi_1} s_1^1 \\ T \downarrow & & \downarrow T_z \quad \downarrow Id \\ x_2 & \xrightarrow{f} & z_2 \xrightarrow{\Pi_1} s_1^2 \end{array} \quad \begin{array}{ccc} x_1 & \xrightarrow{f} & z_1 \xrightarrow{\Pi_2} s_2^1 \\ T \downarrow & & \downarrow T_z \quad T_{s_2} \downarrow \\ x_2 & \xrightarrow{f} & z_2 \xrightarrow{\Pi_2} s_2^2 \end{array}$$

Figure 2. Commutative diagrams describing the relation between the transformation  $T$  applied on  $\mathcal{M}$  that moves  $x_1$  to  $x_2$ , the corresponding transformation  $T_z$  on  $\mathcal{Z}$ , and after the projections  $\Pi_1$  (left diagram) and  $\Pi_2$  (right diagram) on the subspaces  $\mathcal{S}_1$  and  $\mathcal{S}_2$  respectively.

**Can we learn disentangled representations?** Our main objective is to obtain a disentangled representation (with respect to Definition 2) without having any access to neither the metrics, nor the manifold  $\mathcal{M} = \mathcal{M}_1 \times \dots \times \mathcal{M}_k$  or its subspaces. We only assume to observe pairs of samples  $(x_1, x_2)$  in the high-dimensional data space  $\mathcal{X}$ .

Our assumption is that w.l.o.g.  $x_2$  results from a transformation of  $x_1, x_2 = T_i(x_1)$ , corresponding to a translation over the submanifold  $\mathcal{M}_i$  for some  $i$ . Moreover, we require that  $(x_1, x_2)$  is invariant to transformations  $T_j$  over  $\mathcal{M}_j \forall j \neq i$ , i.e. the distance of the projection of the sampled pair on the corresponding submanifolds  $\mathcal{M}_j$  is zero  $\forall j$ .<sup>1</sup>

Then, our objective is to learn a mapping  $f : \mathcal{X} \rightarrow \mathcal{Z}$  where  $\mathcal{Z}$  is a low-dimensional product space which acts as a parametric space for  $\mathcal{M}$  via  $g$ , reflecting its structure. Therefore, the mapping  $f$  composed with the projections  $\Pi_i \forall i \in 1, \dots, k$  must be *invariant* with respect to transformations  $T_j$ , and *equivariant* with respect to the transformation  $T_i$ .

The titular question is answered in the following.

**Relation with (Locatello et al., 2020a).** The theoretical setting of Locatello et al. (2020a) is a special case of our framework, where their  $\mathcal{S}_i$  are only 1-dimensional, the  $s \in \mathcal{S}_i$

<sup>1</sup>In practice, we relax this assumption to the case where multiple transformations can occur at the same time, i.e.  $x_2 = T^*(x_1)$ , where  $T^* = T_1 \circ \dots \circ T_k$  and at least one  $T_i = Id, i = 1 \dots k$

parametrize a fixed (typically Gaussian) distribution  $P(s_i)$ , and  $d(a, b) = KL(P(s') || P(s)) \forall s, s' \in \mathcal{S}$  is the Kullback-Leibler divergence. Assuming to have a sufficiently dense sampling of the data, and given that the map  $g$  in Definition 2 is a diffeomorphism, these conditions are sufficient to prove identifiability for our model, reconnecting to the exact case proved in Locatello et al. (2020a).

### 3. Method

To implement our framework in practice, we model  $f$  and  $g$  with an encoder-decoder network, where the encoder  $f \approx g^{-1}$ . We impose the product space structure  $\mathcal{Z} = \mathcal{S}_1 \times \dots \times \mathcal{S}_k$  on  $\mathcal{Z}$  by adding a projection module in the latent space. This module is composed of nonlinear operators  $P_i \forall i \in 1, \dots, k$ , one for each factor of variation (we discuss the choice of  $k$  in the experimental section). The  $P_i$  act as nonlinear projectors, mapping from an *entangled*, intermediate latent space  $\tilde{\mathcal{Z}}$  onto the *disentangled* subspaces  $\mathcal{S}_i \subset \mathcal{Z}$ . We remark that the subspaces  $\mathcal{S}_i$  act as parametric spaces for the latent submanifolds  $\mathcal{M}_i \subset \mathcal{M}$ , where each  $\mathcal{M}_i$  characterizes a single factor of variation. The overall architecture is illustrated in Figure 3.

As we model  $\mathcal{Z} = \mathcal{S}_1 \times \dots \times \mathcal{S}_k$  as a product vector space, a latent vector in  $\mathcal{Z}$  is obtained by aggregating the subspaces through a concatenation operation. Note that, in principle, the subspaces  $\mathcal{S}_i$  could have different dimensionalities, which we are interested in learning. In practice, we set the same dimensionalities  $dim(\mathcal{S}_i) = dim(\mathcal{Z}) = dim(\tilde{\mathcal{Z}})$  for each subspace  $\mathcal{S}_i$  and add a sparsity and orthogonality constraint to them, enforced by a specific term in our loss function. This results in the projectors  $P_i$  mapping onto disjoint subsets of the dimension indices for each subspace, thus allowing us to approximate the concatenation operation through the sum of the subspaces (proof in Appendix), which corresponds to set the operator  $aggr = +$ . We remark that other choices for  $aggr$  may be possible according to the desired structure to impose on  $\mathcal{Z}$ . In the following we describe individually the terms composing our loss function, detailing how each of them contributes to obtain a disentangled representation of the data.

#### 3.1. Losses

We model  $f$  and  $g$  as neural networks parametrized by a set of parameters  $\theta$  and  $\gamma$  respectively, while the nonlinear operators  $P_i$  are parametrized by  $\omega_i$ . The model is trained by minimizing the composite energy  $\mathcal{L}$ :

$$\mathcal{L} = \mathcal{L}_{rec} + \beta_1(\mathcal{L}_{dis} + \mathcal{L}_{spar}) + \beta_2\mathcal{L}_{cons} + \beta_3\mathcal{L}_{reg} \quad (1)$$

balanced by regularization parameters  $\beta_1, \beta_2, \beta_3$ . We minimize  $\mathcal{L}$  w.r.t to the parameters  $\theta, \gamma, \omega_i$ .

For each of these terms, we now provide an explicit formula

and describe their role in the optimization.

#### Reconstruction loss

$$\mathcal{L}_{rec} = \|x - g_\gamma(\text{aggr}(P_{1,\omega_1}f_\theta(x), \dots, P_{k,\omega_k}f_\theta(x)))\|_2^2 \quad (2)$$

The reconstruction term captures the global structure of the manifold  $\mathcal{M}$  by enforcing  $f \approx g^{-1}$ . We remark that invertibility also implies bijectivity on the data manifold.

#### Consistency losses

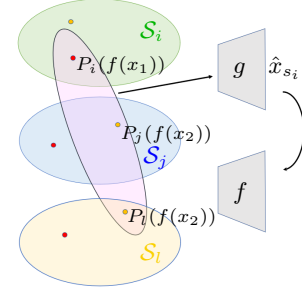
$$\mathcal{L}_{cons} = \sum_{i=1}^k \|P_{i,\omega_i}(f_\theta(\hat{x}_{s_i})) - s_i\|_2^2, \quad (3)$$

where  $s_i = P_i(f(x_1))$  and

$$\hat{x}_{s_i} = g(\text{aggr}(P_i(f(x_1)), P_l(f(x_2)), \dots, P_j(f(x_2))))$$

$\forall j, l \in 1, \dots, k$ , with  $l \neq i$  and  $j \neq i$ . The minimization of this loss makes the nonlinear operator  $P_i$  invariant to changes in the subspaces  $\mathcal{S}_j, \forall j \neq i$ .

This invariance is induced by aggregating, at training time, the representations  $P_i(x_1)$  with the images of  $x_2$  through  $P_j, \forall j \neq i$  in the latent space  $\mathcal{Z}$ . This combination creates a new latent vector that differs from the encoding of  $x_1$  only in the subspaces



$\mathcal{S}_j, \forall j \neq i$  as illustrated in the inset Figure. Forcing  $P_i(f(x_1))$  and the image of the resulting latent vector via the composition  $P_i \circ f \circ g$  to coincide in  $\mathcal{S}_i$ , is equivalent to require that  $P_i$  is invariant to changes in the other subspaces  $\mathcal{S}_j$ ; this promotes injectivity of the  $P_i$ .

**Distance loss.** This term, defined below, ensures the second property of Definition 2 and therefore, coupled with the consistency constraint, is the key loss for constraining disentanglement in the representation.

Given a pair  $(x_1, x_2)$  and its latent representation  $(z_1, z_2)$ , assume the existence of an oracle  $\mathcal{O}$ , that, acting on the latent vectors, tells us exactly which subspace  $\mathcal{S}_i$  of  $\mathcal{Z}$  contains the difference in the input pair. If  $x_2 = T_i(x_1)$  for a fixed  $T_i$  acting on  $\mathcal{M}_i$  then  $\mathcal{O}(\tilde{z}_1, \tilde{z}_2) = i$ . The oracle  $\mathcal{O}$  has been implemented in practice in (Zhan et al., 2019; Locatello et al., 2020b) by allowing a higher degree of supervision, i.e. by incorporating labels into the sampled data pairs. However, in real settings, typically we do *not* have access to labels, thus  $\mathcal{O}$  has to be estimated.

To estimate  $\mathcal{O}$  in our weakly-supervised setting, we proceed as follows: (i) We compute a measure of similarity between the projected pair  $d(s_1^i, s_2^i)$  in each subspace  $\mathcal{S}_i$ ; (ii) we estimate the oracle as  $\tilde{\mathcal{O}}(\tilde{z}_1, \tilde{z}_2) =$

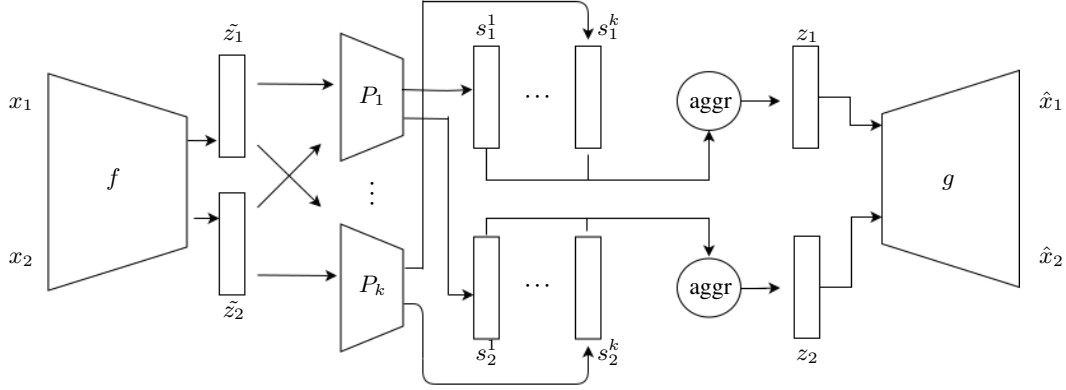
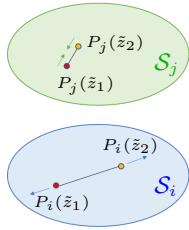


Figure 3. The architecture of our model. We process data in pairs  $(x_1, x_2)$ , which are embedded into an intermediate lower dimensional space  $\tilde{\mathcal{Z}}$  via a siamese network  $f$ . The image  $(z_1, z_2)$  is then mapped into  $k$  smaller spaces  $S_1, \dots, S_k \subset \mathcal{Z}$  via the nonlinear operators  $P_i$ . The resulting vectors are aggregated in  $\mathcal{Z}$ , with  $aggr = +$ , and mapped back to the input data space by the decoder  $g$ . As we do not impose any constraint on  $f$  and  $g$ , the intermediate module of the proposed architecture can be in principle attached to any autoencoder model.

$\arg \max_i d(P_i(\tilde{z}_1), P_i(\tilde{z}_2))^2$ , that corresponds to the subspace  $\mathcal{S}_i$  where the projections differ the most. The measure of similarity in (i) should be general enough to be compared in the different subspaces. We select the squared Euclidean distance normalized by the average length of a vector in each subspace to provide a reliable measure, also considering different dimensions. We indicate with  $\delta_i = d(P_{i,\omega_i}(\tilde{z}_1), P_{i,\omega_i}(\tilde{z}_2))$  the distance between the images on the  $i$ -th subspace,  $\forall i \in 1, \dots, k$ .

We constrain the images onto the subspaces not selected by  $\tilde{\mathcal{O}}$  to be close to each other, because they should ideally correspond to the same point as visualized in the inset Figure.

To avoid the collapse of multiple subspaces into a single point, we insert a contrastive term (Hadsell et al., 2006) to balance the loss, which encourages the projected points in  $\mathcal{S}_i$  to move away from each other. The resulting distance loss is therefore written as:



$$\mathcal{L}_{dis} = \sum_{i=1}^k (1 - \alpha_i) \delta_i^2 + \alpha_i \max(m - \delta_i, 0)^2 \quad (4)$$

where  $\alpha_i = 1$  if  $\tilde{\mathcal{O}}(\tilde{z}_1, \tilde{z}_2) = i$  and  $\alpha_i = 0$  otherwise;  $m$  is a fixed margin, which constrains the points to be at least at distance  $m$  from each other, and prevents the contrastive term from being unbounded.

### Sparsity Loss

$$\mathcal{L}_{spar} = \sum_{i=1}^k \|P_{i,\omega_i}(f_\theta(x)) \odot \sum_{j \neq i}^k P_{j,\omega_j}(f_\theta(x))\|_1 \quad (5)$$

Where  $\odot$  denotes the element-wise product.

This loss combines an orthogonality and an  $\ell_1$ -sparsity constraint on the latent subspaces. It allows us to set only the dimensionality of the latent space  $\mathcal{Z}$  as a hyperparameter, while the algorithm infers the dimensionalities of the subspaces  $\mathcal{S}_i, \forall i$ . Minimizing this energy we force the images of the  $P_i$  to have few non-zero entries. This, together with choice of the sum as aggregation operator for the  $\mathcal{S}_i, i = 1 \dots k$ , imposes the structure of a Cartesian product space on  $\tilde{\mathcal{Z}} = \mathcal{S}_1 \times \dots \times \mathcal{S}_k$ , as we prove in the Appendix. Furthermore, this loss is equivalent to set a constraint on the size of the learned latent space, which is needed to prevent unbounded optimization.

**Training strategy.** We train in two phases. First, we aim to learn the global structure of the manifold, relying solely on the reconstruction loss. Once we have given a structure to the latent space, we can start factorizing it into subspaces as the other terms in the loss enter the minimization.

It is crucial that the space  $\tilde{\mathcal{Z}}$  will also continue to change as the other losses take over, since decoupling completely the reconstruction from the disentanglement could lead to not-separable spaces. The regularization parameters  $\beta_i, i = 1, 2, 3$  are used to impose this behavior. For further details, we refer to the Appendix.

**Regularization loss.** In the first phase of the training, where we mainly aim to achieve good reconstruction quality, we have no guarantees that the information of the factors of variation is correctly spread among the subspaces, and this may lead to a single subspace encoding multiple factors of variation. To avoid this problem, we introduce a penalty which ensures that the choice of the oracle  $\tilde{\mathcal{O}}$  is equally distributed among the subspaces. In practice, the indicator variables in Eq.4 are approximated in each batch of  $N$  samples with a matrix  $\mathbf{A}$  of dimensions  $N \times k$ , obtained by

applying a weighted softmax to the distance matrix of pairs in each of the  $k$  subspaces. This matrix acts as a differentiable mask that implements the oracle  $\tilde{O}$  in practice. In the reconstruction phase, we activate a penalty on the matrix:

$$\mathcal{L}_{reg} = \sum_{j=1}^k \left( \frac{1}{N} \sum_{n=1}^N \mathbf{A}_{n,j} - \frac{1}{k} \right)^2 \quad (6)$$

which ensures that the selection of each subspace has the same probability.

## 4. Experimental results

To validate our model we perform experiments on both synthetic and real datasets. In the synthetic experiments, observations are generated as a deterministic function of the known factors of variation. For the real settings, since the data are collected directly from real observations, the parametric function generating the data is not known, and could have a different number of parameters than the number of factors that we aim to disentangle. To put ourselves in a setting comparable to the competing methods, in all our experiments we use a latent space of dimension  $d = 10$ , unless otherwise specified, and  $k = 10$  latent subspaces.

**Synthetic data.** We adopted 4 widely used synthetic datasets in order to evaluate the effectiveness of our method, namely *DSprites* (Higgins et al., 2017), *Shapes3D* (Kim & Mnih, 2019), *Cars3D* (Reed et al., 2015), *SmallNORB* (LeCun et al., 2004). All these datasets contain images that are parametrically rendered based on some known factors of variation, the goal is thus to obtain a disentangled latent space that reflects these parameters. We resized the input images to a dimension of  $64 \times 64$  pixels. During training we give as input to our method two images which differ just for a single randomly sampled factor of variation, and this is the *only* assumption that we make on the input data. Note that we do not provide any information on which of the factors is changing between the two images. We show quantitative results on these datasets in Tables 1,2,3,4 comparing our method to the state-of-the-art model Ada-GVAE of (Locatello et al., 2020a), in terms of the metrics described in the relative section.

**Real data.** As a benchmark for real data we choose to test our method on FAUST (Bogo et al., 2014), a dataset composed by 100 3D human scans of 10 subjects in 10 different poses. Differently from the synthetic case, the data does not derive from a parametric model. This dataset is particularly challenging, since each of the two factors of variation (pose and identity) is difficult to embed in a 1-dimensional space; indeed, human parametric models define pose and identity using dozens of parameters (Loper et al., 2015). To speedup the training, we remeshed each shape to 2.5K points.

Table 1. Comparison of median disentanglement scores on Shapes3D.

METRIC	$\beta$ -VAE	$\beta$ -TCVAE	Ada-GVAE	Ours
BetaVAE	98.6%	99.8%	<b>100%</b>	<b>100%</b>
FactorVAE	83.9%	86.8%	<b>100%</b>	<b>100%</b>
DCI Disent.	58.8%	70.9%	94.6%	<b>99.0%</b>
MIG	22.0%	27.1%	56.2%	<b>63.7%</b>
MIG-PCA	-	-	-	73.5%
MIG-KM	-	-	-	69.2%

Table 2. Comparison of median disentanglement scores on DSprites.

METRIC	$\beta$ -VAE	$\beta$ -TCVAE	Ada-GVAE	Ours
BetaVAE	82.3%	86.4%	92.3%	<b>98.9%</b>
FactorVAE	66.0%	73.6%	84.7%	<b>88.5%</b>
DCI Disent.	18.6%	30.4%	47.9%	<b>49.7%</b>
MIG	10.2%	18.0%	<b>26.6%</b>	25.7%
MIG-PCA	-	-	-	20.9%
MIG-KM	-	-	-	17.9%

Table 3. Comparison of median disentanglement scores on Cars3D.

METRIC	$\beta$ -VAE	$\beta$ -TCVAE	Ada-GVAE	Ours
BetaVAE	100%	100%	<b>100%</b>	<b>100%</b>
FactorVAE	87.9%	90.2%	<b>90.2%</b>	89.9%
DCI Disent.	22.5%	27.8%	<b>54.0%</b>	48.9%
MIG	8.8%	12.0%	15.0%	<b>25.9%</b>
MIG-PCA	-	-	-	20.6%
MIG-KM	-	-	-	17.8%

Table 4. Comparison of median disentanglement scores on SmallNorb.

METRIC	$\beta$ -VAE	$\beta$ -TCVAE	Ada-GVAE	Ours
BetaVAE	74.0%	76.5%	87.9%	<b>99.2%</b>
FactorVAE	49.5%	54.2%	55.5%	<b>88.2%</b>
DCI Disent.	28.0%	30.2%	33.8%	<b>49.4%</b>
MIG	21.4%	21.0%	25.6%	<b>25.8%</b>
MIG-PCA	-	-	-	20.8%
MIG-KM	-	-	-	17.8%

**Evaluation metrics.** To quantitatively evaluate our experiments we adopt a set of evaluation metrics widely used in the disentanglement literature: namely the  $\beta$ -VAE score and the Factor VAE score, which measure disentanglement as the accuracy of a linear classifier that predicts the index of a fixed factor of variation and a majority vote classifier respectively (Higgins et al., 2017; Kim & Mnih, 2019); the DCI disentanglement score, which measures the entropy of the distribution on the single dimension of the representation vector (Eastwood, 2018); and the mutual information gap (MIG) (Chen et al., 2019) which for each dimension of the representation vector, first measures the mutual information w.r.t. the other dimensions and then takes the

gap between the highest and second coordinate. Note that the aforementioned metrics have been defined to measure the disentanglement in a variational framework, wherein the factors of variation are assumed to be one-dimensional. This is not the case in our method, where each disentangled subspace is *not* required to be one-dimensional. Nevertheless, we can still apply these metrics in the aggregated latent space. This allows us to perform a direct comparison with methods working in the variational setting.

We also introduce two new metrics, which adapt the Mutual Information Gap (MIG) score to a multi-dimensional space. The former, which we denote by MIG-PCA, projects the latent subspaces onto the principal axis of variation through PCA (F.R.S., 1901). This way we can directly reconduct ourselves to the variational setting, where each factor is encoded by just one dimension of the latent space, and use directly the MIG score. The latter, denoted MIG-KM, is based on the use of k-means in the multi-dimensional subspace to derive a one-dimensional discrete random variable. In practice, on each subspace, we extract  $b$  centroids using k-means on the considered evaluation samples. Each sample is then assigned to one of these  $b$  centroids, thus deriving a probability distribution over the centroids. The Mutual Information is then computed between this distribution and the distribution of the ground-truth labels in order to derive the MIG score. This latter metric is particularly important in the real data scenario, where each factor of variation is likely to be multi-dimensional, while MIG-PCA still assumes the factor of variation to be represented in a linear subspace.

**Implementation details.** We performed our experimental evaluation on a machine equipped with an NVIDIA RTX 2080ti, within the Pytorch framework. The architecture for encoder and decoder on images are convolutional, with the same exact settings as (Locatello et al., 2020a). For the experiments on FAUST we used a PointNet (Qi et al., 2017) architecture and a simple MLP as a decoder. Detailed information on the architecture, including the hyperparameter choice, are reported in the Appendix.

#### 4.1. Analysis

We now analyze the core properties of our approach. Additional experiments are reported in the Appendix.

**Inferring the number of latent subspaces.** We stress that our method is tailored for learning the number of subspaces, and therefore the number of generative factors, as well as the dimensionality of each of them. The only hyperparameter that needs to be set is the dimensionality of the latent space  $\mathcal{Z}$  to be factorized. To infer the number of subspaces we over estimate this parameter, with the desirable consequence that the network will activate only some of them, corresponding to the number of ground truth generative factors. The remaining ones will collapse to a point, as we can

observe in the qualitative example of Figure 5.

#### Expressiveness of higher dimensional latent subspaces.

We further report experimental evidence that having multi-dimensional subspaces allows to obtain a better disentangled representation. We show this on the challenging FAUST dataset (Bogo et al., 2014), where the factors of variation are not reducible to just one dimension. As a test for our method, we confront ourselves with the challenging task of separating pose and style for human 3D models in different poses and identities.

In Table 5 we ran this experiment while growing progressively the dimensionality of the latent space  $\mathcal{Z}$  from 2 to 16. Crucially, we show that adopting progressively larger multi-dimensional subspaces does not degrade the disentanglement quality as measured by the MIG-KM score, while the reconstruction error goes down faster than with one dimension. The standard MIG score shows that in the one-dimensional case the performance of disentanglement degrades. A qualitative comparison on a different dataset is also shown in Figure 4.

We remark here that the constraint of observing data sampled in pairs is a reasonable assumption, because data come often in this form in the acquisition stage; examples include temporal consistency of video frames (Lai et al., 2018), object identity consistency of a rendered object from different camera angles, etc.

Table 5. Comparison of disentanglement metrics and reconstruction score at varying latent space dimensions on the FAUST dataset. We trained our model by fixing the number of latent subspaces to 2, while allowing different dimensions of the global latent space to 2, 4, 8, 16.

		MIG			
		2	4	8	16
Ada-GVAE		15.1%	<b>11.1%</b>	<b>4.6%</b>	2.3%
Ours		<b>18.2%</b>	4.39%	3.08%	<b>2.68%</b>
		MIG-KM			
		2	4	8	16
Ours		-	10.6%	10.3%	9.5%
		Reconstruction error			
		2	4	8	16
Ada-GVAE		7.22e-3	5.11e-3	3.39e-3	3.30e-3
Ours		<b>2.56e-3</b>	<b>2.04e-3</b>	<b>1.24e-3</b>	<b>1.26e-3</b>

#### Robustness to simultaneous changes of multiple factors.

Despite the proposed framework assumes that the observed pairs change in only one factor of variation, we show that in practice our method performs very well also in settings where more than one factor may vary simultaneously and in a random fashion. The only assumption we make is that at least one factor is shared among the elements of the sampled

Table 6. Performance comparison of our method with and without fixing the number of changing factors to exactly one. We report median results on the *Shapes3D* dataset.

#factors	Beta VAE	DCI Dis.	MIG	MIG-PCA	MIG-KM
One	100%	99.0%	63.7%	73.5%	69.2%
Variable	98.9%	94.9%	62.3%	70.5%	66.9%

pairs. To build the pairs of observations we follow the same process as before, where we sample not one, but a random number between 1 and  $k - 1$  transformed factors between the elements of the sampled pair. Our method proves to be very robust to this challenging setting, with performance comparable to the case with one fixed factor of variation, as we show in Table 6.

## 5. Conclusions

In this paper, we introduce a new definition of disentanglement based on the notion of metric space, which generalizes existing approaches. Relying on this definition, we propose a simple recipe to compute disentangled representations in practice, in a weakly supervised setting. In contrast with previous work, we demonstrate that disentanglement representations benefit from the choice of modelling generative factor as possibly multi-dimensional subspaces, especially when the true factors of variation live in a space with dimension greater than 1. In many cases, the proposed solution outperforms state-of-the-art competitors on synthetic datasets and more challenging real-world scenarios. Moreover, our method can be easily adapted to many standard neural network models as a plugin module.

**Future work.** Exploiting the possible contribution of the proposed model in existing autoencoders is a natural direc-

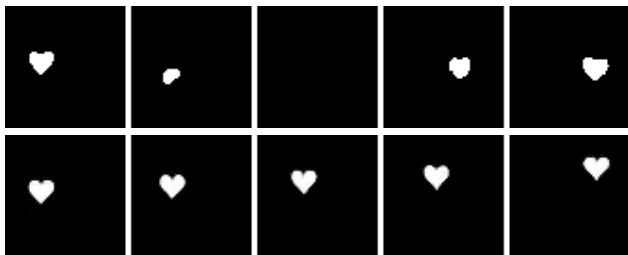


Figure 4. Interpolation example on the prevalent latent dimension / subspace of the changing factor on a pair of images from *Dsprites*; we compare Ada-GVAE (top) with our method (bottom). To highlight the importance of having multi-dimensional disentangled subspaces, we trained the network by aggregating the translation factors along the  $x$  and  $y$  dimensions into a single one, making it multi-dimensional by construction. Even if reaching a similar MIG score (Ada-GVAE: 50.2%, Ours: 49.3%), the interpolation obtained with our method is more well behaved.

tion raised by this paper. In the future, we aim to investigate possible alternative constraints to incorporate additional properties in the latent space or its factorization, e.g. by modelling  $\mathcal{Z}$  as a product of curved spaces, similarly to (Gu et al., 2019).

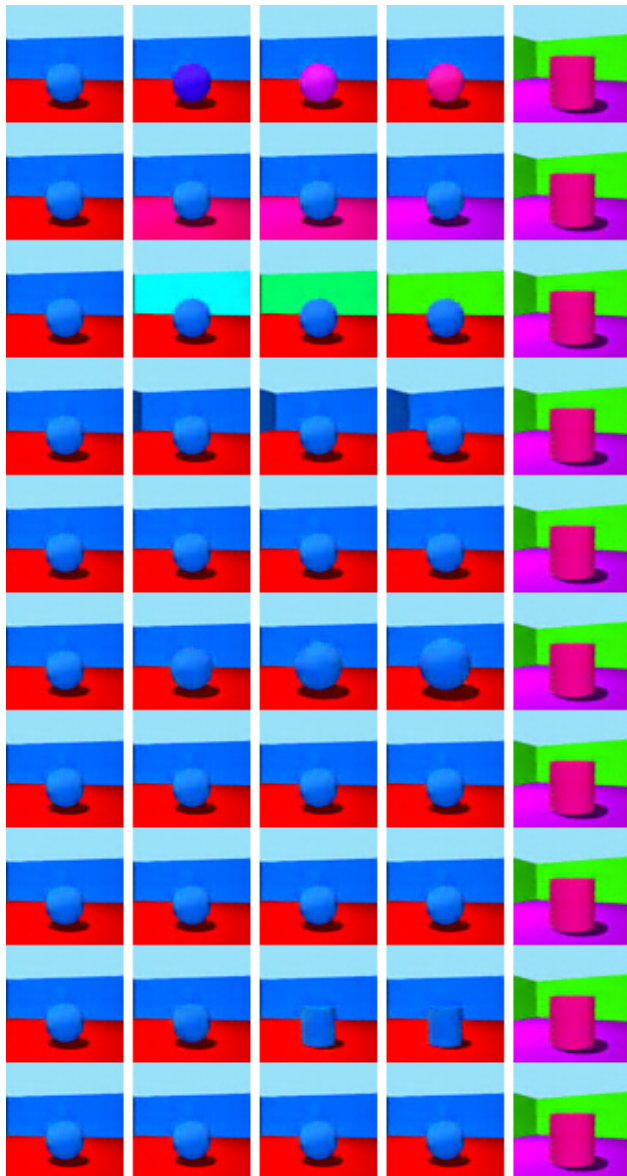


Figure 5. We show a qualitative result of interpolation in latent subspaces on *3Dshapes* between a pair of samples that differ on every factor of variation. The source image on the left column is linearly interpolated (middle columns) in each latent subspace, to reach the target image (rightmost column). We show how every factor of variation (hue of the object, hue of floor, hue of the wall, camera angle, object size, object shape) is correctly modelled by one subspace (respectively rows 1,2,3,4,6,9) while the subspaces corresponding to the other rows (5,7,8,10) do not model any factor and collapse to a single point.



## Acknowledgements

The authors are supported by the ERC Starting Grant No. 802554 (SPECGEO) and the MIUR under grant “Dipartimenti di eccellenza 2018-2022” of the Department of Computer Science of Sapienza University.

## References

- Belkin, M. and Niyogi, P. Laplacian eigenmaps and spectral techniques for embedding and clustering. In Dietterich, T., Becker, S., and Ghahramani, Z. (eds.), *Advances in Neural Information Processing Systems*, volume 14, pp. 585–591. MIT Press, 2002.
- Bengio, Y., Courville, A., and Vincent, P. Representation learning: A review and new perspectives. *arXiv 1206.5538*, 2014.
- Bogo, F., Romero, J., Loper, M., and Black, M. J. FAUST: Dataset and evaluation for 3D mesh registration. In *Proceedings IEEE Conf. on Computer Vision and Pattern Recognition (CVPR)*, Piscataway, NJ, USA, June 2014. IEEE.
- Chen, R. T. Q., Li, X., Grosse, R., and Duvenaud, D. Isolating sources of disentanglement in variational autoencoders. *arXiv 1802.04942*, 2019.
- Comon, P. Independent component analysis, a new concept? *Signal Processing*, 36(3):287 – 314, 1994. Higher Order Statistics.
- Eastwood, C. A framework for the quantitative evaluation of disentangled representations. In *Proc. ICLR*, 2018.
- F.R.S., K. P. Liii. on lines and planes of closest fit to systems of points in space. *The London, Edinburgh, and Dublin Philosophical Magazine and Journal of Science*, 2(11): 559–572, 1901. doi: 10.1080/14786440109462720.
- Gu, A., Sala, F., Gunel, B., and Ré, C. Learning mixed-curvature representations in product spaces. In *ICLR*, 2019.
- Hadsell, R., Chopra, S., and Lecun, Y. Dimensionality reduction by learning an invariant mapping. pp. 1735 – 1742, 02 2006. ISBN 0-7695-2597-0. doi: 10.1109/CVPR.2006.100.
- Higgins, I., Matthey, L., Pal, A., Burgess, C., Glorot, X., Botvinick, M., Mohamed, S., and Lerchner, A. beta-vae: Learning basic visual concepts with a constrained variational framework. In *ICLR*, 2017.
- Higgins, I., Amos, D., Pfau, D., Racanière, S., Matthey, L., Rezende, D. J., and Lerchner, A. Towards a definition of disentangled representations. *ArXiv*, abs/1812.02230, 2018.
- Hyvarinen, A. and Morioka, H. Unsupervised feature extraction by time-contrastive learning and nonlinear ica. In *Proc. NIPS*, 2016.
- Hyvarinen, A., Sasaki, H., and Turner, R. E. Nonlinear ica using auxiliary variables and generalized contrastive learning. *arXiv 1805.08651*, 2019.
- Hyvärinen, A. and Pajunen, P. Nonlinear independent component analysis: Existence and uniqueness results. *Neural Networks*, 12(3):429 – 439, 1999. ISSN 0893-6080. doi: [https://doi.org/10.1016/S0893-6080\(98\)00140-3](https://doi.org/10.1016/S0893-6080(98)00140-3).
- Kazemi, H., Iranmanesh, S. M., and Nasrabadi, N. Style and content disentanglement in generative adversarial networks. In *2019 IEEE Winter Conference on Applications of Computer Vision (WACV)*, pp. 848–856, 2019. doi: 10.1109/WACV.2019.00095.
- Kim, H. and Mnih, A. Disentangling by factorising. *arXiv 1802.05983*, 2019.
- Kumar, A., Sattigeri, P., and Balakrishnan, A. Variational inference of disentangled latent concepts from unlabeled observations. *arXiv 1711.00848*, 2018.
- Lai, W., Huang, J., Wang, O., Shechtman, E., Yumer, E., and Yang, M. Learning blind video temporal consistency. *CoRR*, abs/1808.00449, 2018.
- LeCun, Y., Fu Jie Huang, and Bottou, L. Learning methods for generic object recognition with invariance to pose and lighting. In *Proceedings of the 2004 IEEE Computer Society Conference on Computer Vision and Pattern Recognition, 2004. CVPR 2004.*, volume 2, pp. II–104 Vol.2, 2004. doi: 10.1109/CVPR.2004.1315150.
- Locatello, F., Bauer, S., Lucic, M., Gelly, S., Schölkopf, B., and Bachem, O. Challenging common assumptions in the unsupervised learning of disentangled representations. *ArXiv*, abs/1811.12359, 2019.
- Locatello, F., Poole, B., Rätsch, G., Schölkopf, B., Bachem, O., and Tschannen, M. Weakly-supervised disentanglement without compromises. *arXiv 2002.02886*, 2020a.
- Locatello, F., Tschannen, M., Bauer, S., Rätsch, G., Schölkopf, B., and Bachem, O. Disentangling factors of variation using few labels. *arXiv 1905.01258*, 2020b.
- Loper, M., Mahmood, N., Romero, J., Pons-Moll, G., and Black, M. J. SMPL: A skinned multi-person linear model. *ACM Trans. Graphics (Proc. SIGGRAPH Asia)*, 34(6): 248:1–248:16, October 2015.
- McInnes, L., Healy, J., and Melville, J. UMAP: Uniform Manifold Approximation and Projection for Dimension Reduction. *arXiv e-prints*, art. arXiv:1802.03426, February 2018.

- Nash, J. The imbedding problem for riemannian manifolds. *Annals of Mathematics*, 63(1):20–63, 1956. ISSN 0003486X.
- Pfau, D., Higgins, I., Botev, A., and Racanière, S. Disentangling by subspace diffusion. *arXiv 2006.12982*, 2020.
- Qi, C. R., Su, H., Mo, K., and Guibas, L. J. Pointnet: Deep learning on point sets for 3d classification and segmentation. *arXiv 1612.00593*, 2017.
- Reed, S. E., Zhang, Y., Zhang, Y., and Lee, H. Deep visual analogy-making. In Cortes, C., Lawrence, N., Lee, D., Sugiyama, M., and Garnett, R. (eds.), *Advances in Neural Information Processing Systems*, volume 28, pp. 1252–1260. Curran Associates, Inc., 2015.
- Roweis, S. T. and Saul, L. K. Nonlinear Dimensionality Reduction by Locally Linear Embedding. *Science*, 290(5500):2323–2326, 2000. doi: 10.1126/science.290.5500.2323.
- Shu, R., Chen, Y., Kumar, A., Ermon, S., and Poole, B. Weakly supervised disentanglement with guarantees. *arXiv 1910.09772*, 2020.
- Tenenbaum, J. B., Silva, V. d., and Langford, J. C. A global geometric framework for nonlinear dimensionality reduction. *Science*, 290(5500):2319–2323, 2000. ISSN 0036-8075. doi: 10.1126/science.290.5500.2319.
- van der Maaten, L. and Hinton, G. Visualizing data using t-sne. *Journal of Machine Learning Research*, 9(86): 2579–2605, 2008.
- Whitney, H. Differentiable manifolds. *Annals of Mathematics*, 37(3):645–680, 1936. ISSN 0003486X.
- Zhan, G., Zhao, Y., Zhao, B., Yuan, H., Chen, B., and Dong, H. DLGAN: disentangling label-specific fine-grained features for image manipulation. *CoRR*, abs/1911.09943, 2019.

## A. Implementation details

For the experiments on the datasets *DSprites* (Higgins et al., 2017), *Shapes3D* (Kim & Mnih, 2019), *Cars3D* (Reed et al., 2015), *SmallNORB* (LeCun et al., 2004), we implement a simple convolutional architecture for both the encoder and the decoder. We report the detailed parameters in Table 7, where  $d$  refers to the dimensionality of the latent space  $\mathcal{Z}$ , which bounds the maximum dimensionality of each of the  $k$  latent subspaces  $\mathcal{S}_1 \dots \mathcal{S}_k$ . The architecture of the nonlinear projectors  $P_i$  is described in Table 9. For the *FAUST* dataset we employ a PointNet (Qi et al., 2017) based architecture for the encoder and a simple MLP for the decoder. Details are reported in Table 8

Table 7. Convolutional architecture used in image datasets.

Encoder	Decoder
Input : $64 \times 64 \times$ number of channels	Input : $\mathbb{R}^d$
$4 \times 4$ conv, 32 ReLU, stride 2, padding 1	FC, 256, ReLU
$4 \times 4$ conv, 32 ReLU, stride 2, padding 1	FC, 256, ReLU
$4 \times 4$ conv, 64 ReLU, stride 2, padding 1	FC, $64 \times 4 \times 4$ , ReLU
$4 \times 4$ conv, 64 ReLU, stride 2, padding 1	$4 \times 4$ upconv, 64 ReLU, stride 2, padding 1
FC, 256, ReLU	$4 \times 4$ upconv, 32 ReLU, stride 2, padding 1
FC, $d$	$4 \times 4$ upconv, 32 ReLU, stride 2, padding 1
-	$4 \times 4$ upconv, number of channels, stride 2, padding 1

Table 8. PointNet - MLP architecture used in FAUST dataset.

Encoder	Decoder
Input : $2500 \times 3$	Input : $\mathbb{R}^d$
$1 \times 1$ conv, 32, BatchNorm, ReLU,	FC, 1024, LeakyReLU
$1 \times 1$ conv, 128, BatchNorm, ReLU,	FC, 2048, LeakyReLU
$1 \times 1$ conv, 256, BatchNorm, ReLU,	FC, $2500 \times 3$ , ReLU
$1 \times 1$ conv, 512,	-
MaxPooling,	-
FC, 512, BatchNorm, ReLU,	-
FC, 256, BatchNorm, ReLU,	-
FC, 128, BatchNorm, ReLU,	-
FC, $d$ ,	-

Table 9. Projectors architecture.

P
Input : $\mathbb{R}^d$
FC $d$ , ReLU
FC $d$

### A.1. Experimental settings

For the comparisons with (Locatello et al., 2020a) and its top performer model Ada-GVAE presented in Tables 1-4 in the main paper, we set the dimensionality  $d$  of the latent space  $\mathcal{Z}$  to 10, and the number of subspaces  $k$  to 10. This puts us in a setting that is as close as possible to (Locatello et al., 2020a), where the latent space is 10-dimensional and the subspaces are 1-dimensional by construction. For all the quantitative experiments we trained 5 times the same model with different random seeds, and report the median results on each dataset. A summary of the hyperparameters are in Table 10.

Parameter	Value
$d$	10
$k$	10
$\beta_1$	0.1
$\beta_2$	100
$\beta_3$	0.0001
Batch Size	32
Optimizer	Adam
Learning rate	0.0005
Adam: (beta1, beta2, epsilon)	(0.9, 0.99, 1e-8)

Table 10. Hyper-parameter settings for the experiments in Table 1-4 of the main paper.

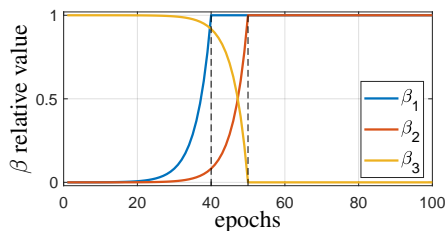


Figure 6. Evolution of the regularization parameters  $\beta_i, i = 1, 2, 3$  as a function of the epoch number. Here, the parameters are all scaled to have a maximal value of one.

## B. Training process

We split the training process in two stages: (i) a *reconstruction phase*, and (ii) a *disentanglement phase*. This strategy helps in obtaining better results; this is due to the fact that our distance loss  $\mathcal{L}_{dis}$  needs to operate in a latent space  $\mathcal{Z}$  already structured, where the distances are meaningful. Moreover, our consistency loss makes use of the reconstructed observations, that have to be well formed to make it relevant. We stress that the two phases are not completely separated, since the space  $\tilde{\mathcal{Z}}$  continues to be optimized during the disentanglement phase.

In practice, we implement this by back-propagating only through the reconstruction loss for the first 20% of the training iterations. Then, the losses enter one after the other in the following order:  $\mathcal{L}_{reg}, \mathcal{L}_{dis}, \mathcal{L}_{cons}$  in a slow-start mode. This is obtained by exponentially increasing the regularization parameters  $\beta_i$  for  $i = 1, 2$  during the training, until they reach their maximal value (as reported in Table 10), with  $\beta_2$  being shifted in time (number of iterations/epochs) with respect to  $\beta_1$ . Conversely, we set  $\beta_3 = (1 - \beta_2)$ , so it exponentially decays until it reaches zero; indeed, the regularization loss prevents the subspace from collapsing until the other losses are active at full capacity. We show an example of the behavior of the  $\beta$ 's in Figure 6.

Loss terms	Rank correlation					
	Beta VAE	Factor VAE	DCI Dis.	MIG	MIG-PCA	MIG-KM
Complete	<b>100%</b>	<b>100%</b>	96.1%	<b>81.0%</b>	<b>86.0%</b>	<b>80.3%</b>
W/o $\mathcal{L}_{reg}$	99.5%	99.8%	77.2%	48.2%	58.6%	51.5%
W/o $\mathcal{L}_{cons}$	<b>100%</b>	97.1%	<b>97.0%</b>	65.4%	81.0%	71.0%
W/o $\mathcal{L}_{reg}, \mathcal{L}_{cons}$	93.4%	87.9%	78.2%	56.2%	55.5%	53.8%

	$\mathcal{L}_{spar}$	$\mathcal{L}_{dis}$	$\mathcal{L}_{cons}$	$\mathcal{L}_{reg}$	$\mathcal{L}_{rec}$
MIG	-27	2	-30	-31	39
MIG-PCA	-44	-7	-54	-43	49
MIG-KM	-45	1	-56	-37	49
DCI	-35	-26	-21	-65	28

Table 11 & Figure 7. Analysis of the importance of the adopted loss terms on the *Shapes3D* dataset. The table (left) reports ablation results; these show the disentanglement scores obtained by training our model with a fixed initialization seed, and removing some of the loss terms. We can see how all the losses contribute to achieve a better disentanglement. A similar conclusion can be drawn looking at the Rank correlation matrix (right), showing the rank correlation between the losses and the disentanglement scores obtained after training 10 models. All the disentanglement losses (first 4 columns) are negatively correlated with disentanglement scores. The disentanglement loss  $\mathcal{L}_{dis}$  seems to be less correlated with respect to the others, which is due to the fact that it always reaches a similar low value in all the runs.

## C. Ablation study

In this section, we justify the importance of the consistency loss and the distribution loss by running ablation experiments on them. We fixed a random seed and experimented with a complete run, a run without the regularization loss, a run without the consistency loss, and lastly a run without both on the *Shapes3D* dataset. The importance of using all our loss terms is highlighted in Table 11, where we report the  $\beta$ -VAE, Factor-VAE, DCI and MIG scores for these setups. This is further supported by the rank correlation matrix between losses and disentanglement scores shown in Figure 7.

## D. Subspace structure

### D.1. The latent subspace structure

The model architecture (Figure 3), imposes a factorized structure on the latent space  $\mathcal{Z}$  into subspaces  $\mathcal{S}_i, i = 1..k$ . In principle, the aggregator operator depicted could be any linear or nonlinear aggregation operation. In our experiments we simply choose to *sum* all the subspaces, for the following reason: due to the sparsity induced on the subspaces by the loss  $\mathcal{L}_{spar}$ , the sum operation provides us with an approximation of the cartesian product, leading to  $\mathcal{Z} \approx \mathcal{S}_1 \times \dots \times \mathcal{S}_k$ . More precisely, if the sparsity constraint holds (*i.e.*  $\mathcal{L}_{spar} = 0$ ), the sum operation will be equivalent to taking the cartesian product on the latent subspace vectors, since on each dimension  $r \in 1 \dots d$  such that  $s_i[r] \neq 0$ , for an  $i \in 1, \dots, k$  the loss  $\mathcal{L}_{spar}$  enforces the latent vectors to have  $s_q[r] = 0 \quad \forall q \neq i \in 1, \dots, k$ . We prove this in the following:

**Sketch of proof.** We prove that the sparsity imposes the structure of a product space on the latent subspace vectors. We do this by studying the first order optimality conditions for  $\mathcal{L}_{spar}$ ,  $\frac{\partial \mathcal{L}_{spar}(s_i)}{\partial s_i} = 0$ , where with  $s_i = P_i(f(x))$  we denote a latent vector in the subspace  $\mathcal{S}_i$ . Indicating with  $\odot$  the element-wise product, we can write:



Figure 8. A visualization of the main variables involved in our proof.

$$\mathcal{L}_{spar} = \sum_{i=1}^k \mathcal{L}_{spar}^{\mathbf{s}_i} = \sum_{i=1}^k \|\mathbf{s}_i \odot \underbrace{\sum_{j \neq i}^k \mathbf{s}_j}_{Q}\|_1, \quad \text{where } \mathcal{L}_{spar}^{\mathbf{s}_i} = \|\mathbf{s}_i \odot \sum_{j \neq i}^k \mathbf{s}_j\|_1. \quad (7)$$

We aim to study  $\frac{\partial \mathcal{L}_{spar}^{\mathbf{s}_i}}{\partial \mathbf{s}_i} = 0, \forall i \in 1, \dots, k$  that is equivalent to:

$$\frac{\partial \mathcal{L}_{spar}^{\mathbf{s}_i}}{\partial \mathbf{s}_i} = \frac{\partial \|Q\|_1}{\partial Q} \frac{\partial Q}{\partial \mathbf{s}_i} = \left( \text{sign}(\mathbf{s}_i \odot \sum_{j \neq i}^k \mathbf{s}_j) \right) \odot \left( \sum_{j \neq i}^k \mathbf{s}_j \right) = 0, \forall i \in 1, \dots, k. \quad (8)$$

W.l.o.g. we fix a dimension  $r \in 1, \dots, d$  in the latent space. By indicating with  $\mathbf{s}_i[r]$  the  $r$ -th entry of  $\mathbf{s}_i$  we can write:

$$\frac{\partial \mathcal{L}_{spar}^{\mathbf{s}_i}}{\partial \mathbf{s}_i}[r] = \left( \text{sign}(\mathbf{s}_i[r] \sum_{j \neq i}^k \mathbf{s}_j[r]) \right) \left( \sum_{j \neq i}^k \mathbf{s}_j[r] \right) = 0. \quad (9)$$

To satisfy Eq. (9), we have three possible cases:

- *Case 1:*  $\mathbf{s}_i[r] = 0$  and  $\sum_{j \neq i}^k \mathbf{s}_j[r] \neq 0$
- *Case 2:*  $\mathbf{s}_i[r] \neq 0$  and  $\sum_{j \neq i}^k \mathbf{s}_j[r] = 0$

Since we are optimizing  $\forall i$  we can consider  $\frac{\partial \mathcal{L}_{spar}^{\mathbf{s}_q}}{\partial \mathbf{s}_q}[r] = 0$  for every other  $q \in 1 \dots k, q \neq i$ , Therefore we have:

$$\frac{\partial \mathcal{L}_{spar}^{\mathbf{s}_q}}{\partial \mathbf{s}_q}[r] = \left( \text{sign}(\mathbf{s}_q[r] \sum_{l \neq q}^k \mathbf{s}_l[r]) \right) \left( \sum_{l \neq q}^k \mathbf{s}_l[r] \right) = 0 \quad (10)$$

We can split this latter case in two subcases:

- *Case 2.1:*  $\mathbf{s}_q[r] = 0, \forall q \neq i$   
Therefore, satisfying our thesis.
- *Case 2.2:*  $\mathbf{s}_q[r] \neq 0$  for at least one  $q \neq i$ .

In this situation, we can write:

$$\sum_{j' \neq q, i}^k \mathbf{s}_{j'}[r] + \mathbf{s}_q[r] = 0 \text{ and thus } \sum_{j' \neq q, i}^k \mathbf{s}_{j'}[r] = -\mathbf{s}_q[r]. \quad (11)$$

From which we have:

$$\sum_{j' \neq q}^k \mathbf{s}_{j'}[r] = \mathbf{s}_i[r] + \sum_{j' \neq q, i}^k \mathbf{s}_{j'}[r] = \mathbf{s}_i[r] - \mathbf{s}_q[r]. \quad (12)$$

Substituting in Eq.10 (by replacing  $j'$  with  $l$ ) we get:

$$\frac{\partial \mathcal{L}_{spar}^{\mathbf{s}_q}}{\partial \mathbf{s}_q}[r] = \left( \text{sign}(\mathbf{s}_q[r] (\mathbf{s}_i[r] - \mathbf{s}_q[r])) \right) (\mathbf{s}_i[r] - \mathbf{s}_q[r]) \quad (13)$$

Now because we have that  $\mathbf{s}_q[r] \neq 0$ , this implies:

$$\frac{\partial \mathcal{L}_{spar}^{s_q}}{\partial \mathbf{s}_q}[r] = 0 \iff \mathbf{s}_i[r] - \mathbf{s}_q[r] = 0 \implies \mathbf{s}_i[r] = \mathbf{s}_q[r] \quad (14)$$

and this holds  $\forall q \in 1, \dots, k$  and  $q \neq i$  such that  $\mathbf{s}_q[r] \neq 0$ . (referring to Figure 8 may help the reader).

This allows us to conclude that:  $\sum_{j \neq i}^k \mathbf{s}_j[r] = \alpha \mathbf{s}_i[r] \neq 0$ , with  $\alpha$  being an integer between 1 and  $k - 1$ . Therefore we get a contradiction with our hypothesis of *Case 2*  $\mathbf{s}_i[r] \neq 0$  and  $\sum_{j \neq i}^k \mathbf{s}_j[r] = 0$ , and thus the unique possible subcase is the former *Case 2.1*.

- *Case 3*:  $\mathbf{s}_i[r] = 0$  and  $\sum_{j \neq i}^k \mathbf{s}_j[r] = 0$

Performing the same analysis done in *Case 2*, in this case we get that  $\forall i \in 1 \dots k \mathbf{s}_i[r] = 0$ . Therefore, all the latent subspace vectors will have the same dimension  $r$  set to zero. In this case, we can consider recursively the other  $k - 1$  dimensions. The case where all dimensions  $r \in 1 \dots k$  are zero, for all  $\mathbf{s}_i, i = 1 \dots k$  is theoretically possible, but we stress this is rather an exotic case that cannot happen in practice, as we comment in the last paragraph below.

Since we have chosen  $r$  w.l.o.g., the same  $s$  true for all dimensions in  $1 \dots d$ . Therefore, we have that each vector  $\mathbf{s}_i$  will be nonzero in the  $l > 0$  dimensions where the other  $\mathbf{s}_j$  are zero. Now setting  $aggr = +$ , we have that the sum corresponds to concatenating the latent subspace vectors along the nonzero dimensions, i.e. taking the cartesian product of the subspace to get an element of  $\mathcal{Z}$ .

**Degenerate case** In the proof we mentioned the degenerate case in which  $\mathbf{s}_i[r] = 0 \forall i \in 1 \dots k, \forall r \in 1 \dots d$ . This would mean that the latent subspaces have collapsed to the same point (a vector made of zeros). This exotic case is never reached in practice, due to the other losses such as the reconstruction loss, the consistency losses, and the contrastive term of the distance loss.

## E. Additional results

**Importance of multidimensional latent subspaces** We remark again the importance of allowing subspaces with dimension  $d > 1$ , which is a key point distinguishing our approach from current methods like (Locatello et al., 2020a; Shu et al., 2020). We show a qualitative result of interpolation on disentangled subspaces on the FAUST dataset, increasing the dimensionality of the factorized latent space  $\mathcal{Z}$  in Figure 9. We can see how, when a single factor represents a complex transformation class, having multidimensional disentangled subspaces allows to better capture the detailed behavior of the input data.

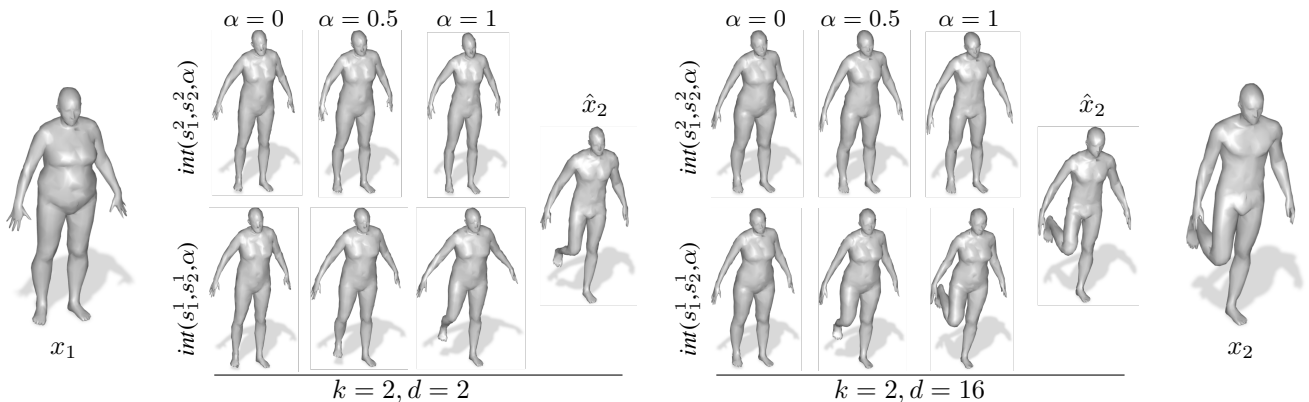


Figure 9. Disentangled interpolation on a pair of FAUST shapes with different dimensions of the latent space. For each of the two latent space dimensions ( $d = 2$  on the left and  $d = 16$  on the right) we encode the two input shapes  $x_1$  and  $x_2$  to their relative subspace latent vectors  $(s_1^1, s_1^2)$  for  $x_1$  and  $(s_2^1, s_2^2)$  for  $x_2$ . We then interpolate separately the 2 latent subspaces between the two shapes, and obtain the decoded shapes  $g(aggr(s_1^1, int(s_1^2, s_2^2, \alpha)))$  (top row) and  $g(aggr(int(s_1^1, s_2^1, \alpha), s_1^2))$  (bottom row), with  $int(a, b, \alpha) = (1 - \alpha)a + \alpha b$ . We can see how, even if both configurations are able to achieve the disentanglement between pose and style of the subjects, the smaller latent space is not able to encode the finer details of the shapes, resulting in smoother and less-accurate reconstructions.

**Analysis of the latent subspaces** To show that our method is capable of inferring the correct number of subspaces, and also to show how properly they are characterized, we perform a qualitative and quantitative analysis on the latent subspaces (Figure 10). We project each latent subspace (approximated by randomly sampling 512 elements in the dataset) onto a 2-dimensional subspace, using the dimensionality reduction technique of (t-SNE) (van der Maaten & Hinton, 2008). We show which subspace encodes information about which factor by counting the number of clusters that are formed by t-SNE. At convergence, the number of clusters will correspond loosely to the number of possible values that the generative factor can assume (e.g. if the true distribution of the generative factor is discrete and 10-dimensional, we expect to count 10 clusters). We can also see that our algorithm is capable of inferring the correct number of subspaces from an overestimate, this reflects in the fact that when a factor does not encode any information it collapses to a single cluster. We accompany each latent subspace projection plot with an interpolation of pair of samples, which differ on each factor of variation on each of the subspace. These results are supported by the quantitative evidence in Table 12, where we measure the average standard deviation in each subspace on the same random sampling plotted in 2 dimensions; we show that there is a strong gap between variance in the subspaces that encode information, and those that are collapsed.

Table 12. Average standard deviation on the latent subspaces corresponding to Figure 10.

Subspace	$\mathcal{S}_1$	$\mathcal{S}_2$	$\mathcal{S}_3$	$\mathcal{S}_4$	$\mathcal{S}_5$	$\mathcal{S}_6$	$\mathcal{S}_7$	$\mathcal{S}_8$	$\mathcal{S}_9$	$\mathcal{S}_{10}$
Average std	0.061	0.043	0.063	0.026	2.6e-5	2.1e-5	1.5e-5	0.058	0.063	2.1e-5

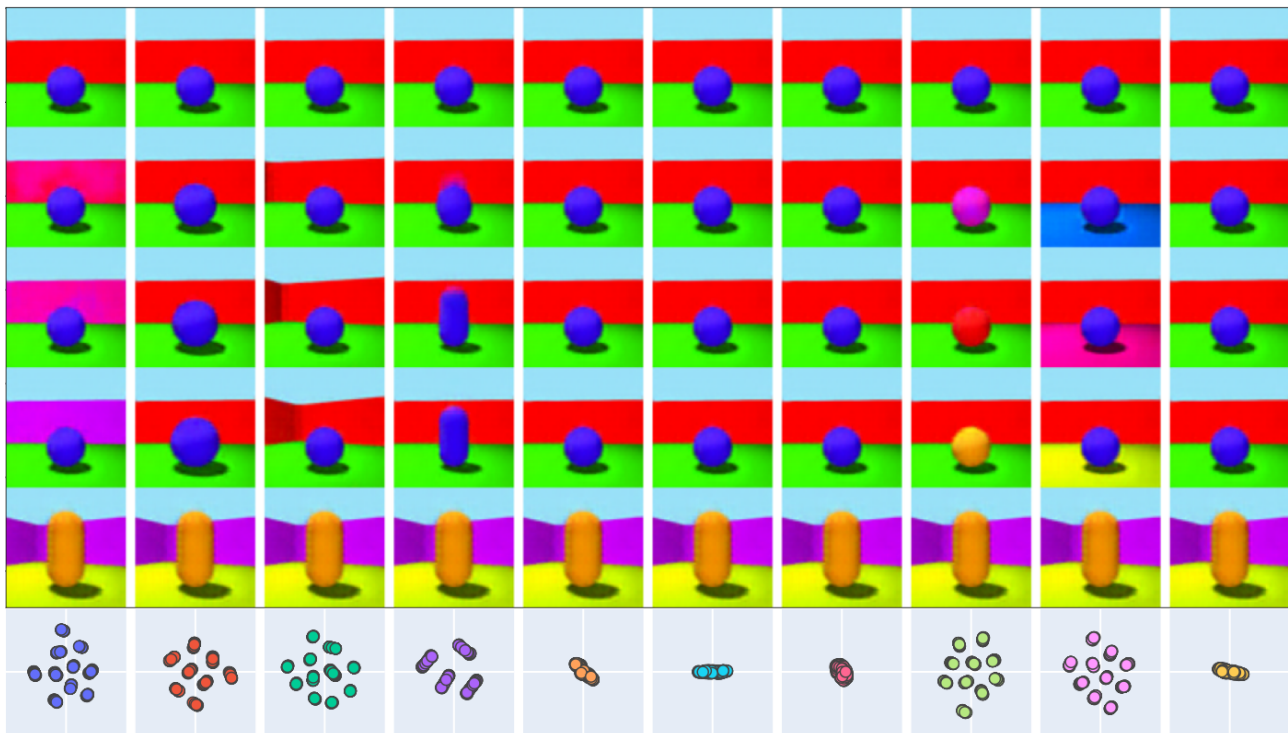


Figure 10. Analysis of the latent subspaces at training convergence on the *Shapes3D* dataset. We project each latent subspace (ordered by column number) on a 2-dimensional space, using t-SNE (last row). On the rows we show the interpolation (rows 2,3,4) between two samples which differ on all factors of variation (rows 1,5). We show that the latent subspaces (columns 1,2,3,4,8,9) which encode information about the generative factors (wall hue, size, camera angle, shape, object hue, floor hue) are correctly characterized by the latent subspace projections, and the number of clusters is almost always equal to the number of possible values that the generative factor can assume. For example, the number of clusters in the first subspace corresponds to the ten possible color hue values for the wall, and the number of clusters in the 4th subspace corresponds to the number of possible shapes in the dataset. The latent spaces which do not encode any information (columns 5,6,7,10) collapse to one point (represented by a single, small cluster in the projection), as confirmed by the quantitative evaluation in Table 12.